First-principles calculations of the atomic structure and electronic states of Li_xFeF_3

Masahiro Mori,[*] Shingo Tanaka,[†] Hiroshi Senoh, Keitaro Matsui,[‡] Toyoki Okumura, and Hikari Sakaebe
Research Institute of Electrochemical Energy, Department of Energy and Environment, National Institute of Advanced Industrial Science and Technology, 1-8-31, Midorigaoka, Ikeda, Osaka 563-8577, Japan

Hisao Kiuchi
Office of Society-Academia Collaboration for Innovation, Kyoto University, Gokasho, Uji, Kyoto 611-0011, Japan

Eiichiro Matsubara
Department of Materials Science and Engineering, Kyoto University, Yoshida, Sakyo, Kyoto 606-8501, Japan

(Received 5 March 2019; revised manuscript received 1 July 2019; published 25 July 2019)

We calculate the atomic and electronic structures of trirutile-type Li_xFeF_3 ($x = 0$, 0.25, 0.5, 0.75, and 1) by first-principles calculations and evaluate the relative stability among the optimized structures by energy analysis. $Li_{0.5}FeF_3$ is more stable than the three-phase coexistence of FeF_3, FeF_2, and LiF, whereas the other compositions are unstable. The analyses of the local electron density, local atomic volume, and local atomic configurations show that the formal valence of Fe atoms decreases from trivalent (3+) to divalent (2+) after Li insertion. In addition, we calculate Fe K-edge x-ray absorption near-edge structure (XANES) spectra in Li_xFeF_3 and compare them with observed spectra. The calculated XANES spectra agree well with the corresponding observed spectra in areas such as the spectral shape and relative position of the main peaks associated with Fe^{3+} and Fe^{2+}. In particular, partial XANES spectra of Fe^{3+} in Li_xFeF_3, for $x = 0.25$, 0.5, and 0.75, have a specific peak between the main peaks, associated with Fe^{3+} and Fe^{2+}. The detailed study reveals that the energy level and intensity ratio of the Fe^{3+} main peaks depend on the adjacent cation site of Fe.

DOI: 10.1103/PhysRevB.100.035128

I. INTRODUCTION

Iron trifluoride (FeF_3) has the potential to perform as an advanced positive electrode material in rechargeable Li batteries, which would enable a high energy density [1,2]. FeF_3 involves strong ionic bonding between Fe and F, and the formal valence of Fe is trivalent (3+); thus, it can operate in a high voltage range. In the application of FeF_3 as a positive electrode material, lithium ions are inserted into FeF_3 in the initial discharge process. The reaction mechanism of the charge-discharge process for FeF_3 is poorly understood, although a number of experimental and theoretical studies have been performed to clarify its electrochemical properties. In this study, we call this stage the "insertion region." In the initial state without Li insertion, FeF_3 has a rhombohedral structure (#167: $R\bar{3}c$), which contains a corner-sharing $FeF_{6/2}$ octahedron, connected to form a three-dimensional tunnel structure [3]. Yamakawa *et al.* proposed a model in which Li ions were inserted through this tunnel structure. In association with the insertion, x-ray diffraction (XRD) experiments have shown that part of the FeF_3 changes from a relatively early stage ($0 < x < 0.5$ in Li_xFeF_3) to a trirutile structure (#136: $P4_2/mnm$) based on the rutile structure, and a two-phase reaction of the trirutile and original rhombohedral structure occurs [4]. The trirutile structure is formed by stacking three rutile unit cells along the c-axis direction, each containing 1/3 of the cationic vacancies at nonadjacent sites. Thus, the trirutile and rutile structures exhibit high crystalline similarity. Other XRD and probability density function (PDF) analyses have revealed a trirutile structure with $x = 0.5$ and confirmed that Li ions are inserted up to $x = 1.0$ maintaining the trirutile structure thereafter [3]. From the viewpoint of a theoretical study, a density functional theory (DFT) calculation shows that it is more stable to use the trirutile structure at $x = 0.25$ or greater, when Li atoms are inserted into FeF_3 [5]. Another DFT calculation suggested that trirutile exists in the single phase as a stable structure when Li ($x = 0.25-0.75$) is inserted into the trirutile structure [6].

X-ray absorption near-edge structure (XANES) spectra contain information regarding the electronic structure and chemical bonding around objective atomic species. Thus, experimental measurements and theoretical simulations have been used in many structural analyses. In XANES observations, a shape change in the Fe K-edge spectra was observed in the Li-insertion region; in particular, the spectra shape observed at $x > 0.5$ is similar to that of FeF_2 [6,7]. FeF_2 has a rutile structure, and the formal valence of Fe is divalent (2)+. When Li is electrochemically inserted into FeF_3, the Li^+ ion and one electron are paired, and the Fe atom in the vicinity of the inserted Li tends to be formally reduced by one electron, i.e., the formal valency of the Fe is reduced. This is consistent with the behavior of the change in the Fe K-edge spectra, shown in the XANES observations, as described previously. In this way, it is extremely useful to

[*]masahiro.mori@aist.go.jp
[†]Corresponding author: swing@ni.aist.go.jp
[‡]Present address: Murata Manufacturing Co., Ltd., Higashikotari, Nagaokakyo-shi, Kyoto 617-8555, Japan

TABLE I. Space groups, optimized lattice constants, and optimized lattice volumes of rhombohedral FeF_3 and rutile-type FeF_2, as well as the effective U for the DFT calculations. Here U_{eff} denotes the effective correlation term U used in the DFT calculations.

Compound	Space group	a [Å]	b [Å]	c [Å]	α [°]	β [°]	γ [°]	Volume [Å^3]	U_{eff} [eV]
FeF_3	$R\bar{3}c$ (#167)	5.296	5.296	13.427	90	90	120	326.13	5.00
FeF_3[a]	$R\bar{3}c$ (#167)	5.277	5.277	13.430	90	90	120	323.90	5.00
FeF_3[b]	$R\bar{3}c$ (#167)	5.1980	5.1980	13.3338	90	90	120	312.00	
FeF_2	$P4_2/mnm$ (#136)	4.781	4.781	3.309	90	90	90	75.62	5.00
FeF_2[c]	$P4_2/mnm$ (#136)	4.8005	4.8005	3.3218	90	90	90	76.55	5.05
FeF_2[d]	$P4_2/mnm$ (#136)	4.6945	4.6945	3.3097	90	90	90	72.94	

[a]Calculation by Li *et al.* [13].
[b]Experiment by Jørgensen and Smith [14].
[c]Calculation by López-Moreno *et al.* [12]
[d]Experiment by Stout and Reed [15].

investigate the chemical bonding state of FeF_3 at a local region using the XANES spectrum to help understand the Li insertion region.

In this study, we calculate the atomic and electronic structures of Li-inserted FeF_3 (Li_xFeF_3) using first-principles calculations, and we discuss the energy stability and detailed local atomic configuration of these structures. In addition, we individually calculate the Fe K edge of XANES for all Fe atoms in Li_xFeF_3 including a comparison with the observed spectra. Our aim is to clarify the insertion region of FeF_3 in the discharge process by revealing the type of the local chemical state and elucidate the charge-discharge mechanism of a high-energy FeF_3 positive electrode.

II. METHOD

We investigate the stable atomic structure and electronic state of FeF_3 using the first-principles projected augmented wave (PAW) method [8,9], implemented in the Vienna *ab initio* simulation package (VASP) [10,11]. First, we carry out the calculations for rhombohedral FeF_3 and rutile-type FeF_2 bulks as a benchmark of the present calculations. Table I lists the calculation results of rhombohedral FeF_3 and rutile-type FeF_2 bulks, with reference to past literature [3,4,12,13].

The values are similar to those reported in previous experiments and theoretical calculations. For the magnetic structure of Fe, in both FeF_3 and FeF_2, an antiferromagnetic arrangement is energetically more stable than a ferromagnetic arrangement, which agrees well with the previously reported results [6,12,16,17].

The structure of Li_xFeF_3 can be treated as that of trirutile because the change from a rhombohedral to trirutile structure seems to occur early, as mentioned in the introduction; thus, we concentrate on the trirutile as structures of Li_xFeF_3 bulks. In this study, each Li_xFeF_3 model ($x = 0.00$, 0.25, 0.50, 0.75, and 1.00) is considered for investigating the differences in Li insertions. The generalized gradient approximation (GGA) + U method is used to account for the strong correlation between the localized electrons in Fe-d orbitals [18,19]. In this study, we use a Hubbard effective parameter $U_{eff} = 5.0$ eV for the Fe atoms. The cutoff energy used for the PAW calculation is 600 eV, and the total energy convergence was confirmed to be within 1.0×10^{-6} eV/atom. The k-points sampling is a $4 \times 4 \times 2$ Monkhorst-Pack-type mesh [20]. The threshold values used for the judgment criteria for the cell size and atomic structure optimizations are 0.1 eV/nm (0.01 eV/Å).

As a first trial, we performed calculations to determine all of the spin alignments of Fe in Li_xFeF_3 using initial atomic configurations. For $x = 0.00$ and 1.00, the antiferromagnetic state is the most stable, i.e., bulk FeF_3 and FeF_2. This can be easily understood as all Fe atoms have the same formal valence, Fe^{3+} ($x = 0.00$ and FeF_3) or Fe^{2+} ($x = 1.00$ and FeF_2). For $x = 0.25$ and 0.75, the ferrimagnetic state is the most stable because the total magnetic moments cannot be completely canceled out by the magnetic moments of the Fe^{2+} and Fe^{3+} atoms. It is noteworthy that the numbers of Fe^{2+} and Fe^{3+} atoms are nonequivalent and indicate the respective values and directions. For $x = 0.50$, the ferrimagnetic state is the most stable in the present calculation, although both ferrimagnetic and antiferromagnetic states are possible as the numbers of Fe^{2+} and Fe^{3+} atoms are equivalent.

Based on the obtained structures for each Li_xFeF_3, we calculate the relative energies to obtain the levels of energy stability and density of states (DOS) to determine the local electronic states. To clarify the change in the local chemical state, we calculate the Fe K-edge XANES spectra by the first-principles full-potential augmented plane wave plus local orbitals (APW + lo) method [21]. In the XANES calculations, an excited atom is usually introduced into the supercell; however, it is necessary to use a sufficiently large supercell, such that the interaction between neighboring excited atoms does not affect the calculation results. In the usual case, the influence of the interaction between excited atoms is negligible when they are separated by approximately 1 nm; however, we adopt this after checking whether there is any effect from the size of the structures considered. For use as reference data, the XANES of rhombohedral FeF_3 and rutile-type FeF_2 bulks are also calculated. The validity of our adopted models is verified by a comparison of the calculated XANES with the experimental values.

III. RESULTS AND DISCUSSION

A. Atomic structures

Table II lists the space group, lattice parameters, and cell volumes of Li_xFeF_3 optimized by first-principles calculations. The initial Li_xFeF_3 structures were modeled based on the

TABLE II. Space groups, optimized lattice constants, and optimized cell volumes of trirutile-type Li_xFeF_3, and the effective U value for the DFT calculations.

x	Space group	a [Å]	b [Å]	c [Å]	α [°]	β [°]	γ [°]	Volume [Å^3]	U_{eff} [eV]
0.00	$P4_2/mnm$ (#136)	4.871	4.871	8.813	90.00	90.00	90.00	209.12	5.00
0.00[a]		4.942	4.942	8.846	90.00	90.00	90.00	216.09	
0.25	$Cmm2$ (#35)	4.808	4.808	9.107	90.35	90.35	90.34	210.51	5.00
0.25[b]		4.765	4.765	9.118	90.00	90.00	90.00	207.00	5.00
0.50	$P4_2nm$ (#102)	4.725	4.725	9.383	90.00	90.00	90.00	209.49	5.00
0.50[a]	$P4_2/mnm$ (#136)	4.756	4.756	9.339	90.00	90.00	90.00	211.23	
0.50[b]	$P4_2/mnm$ (#136)	4.726	4.726	9.222	90.00	90.00	90.00	206.00	5.00
0.50[c]	$P4_2/mnm$ (#136)	4.673	4.673	9.290	90.00	90.00	90.00	202.87	
0.50[d]	$P4_2nm$ (#102)	4.679	4.679	9.324	90.00	90.00	90.00	204.13	
0.50[e]	$P4_2nm$ (#102)	4.666	4.666	9.253	90.00	90.00	90.00	201.45	4.00
0.75	$P2$ (#3)	4.859	4.795	9.392	90.00	90.00	89.17	218.80	5.00
0.75[b]		4.878	4.792	9.354	90.00	90.00	90.00	218.64	5.00
1.00	$Pnnm$ (#58)	4.950	4.859	9.212	90.00	90.00	90.00	221.58	5.00
1.00[b]		4.870	4.963	9.201	90.00	90.00	90.00	222.39	5.00

[a]Calculation by Doe *et al.* [5].
[b]Calculation by Zheng *et al.* [6].
[c]Experiment by Portier *et al.* [22].
[d]Experiment by Fourquet *et al.* [23].
[e]Calculation by Lin *et al.* [24].

trirutile-type $Li_{0.5}FeF_3$ structure that was reported in previous experiments [22] as a $P4_2/mnm$ space group. The structures of $x = 0.00$ and 0.25 were modeled by removing Li atoms from $Li_{0.5}FeF_3$ and those of $x = 0.75$ and 1.00 were modeled by inserting Li atoms into interstitial sites (ISs) in $Li_{0.5}FeF_3$. The most energetically stable structures were adopted for each Li_xFeF_3 structure. The present lattice parameters and cell volumes for Li_xFeF_3 are sufficiently reasonable compared with previous calculations [5,6] and experiments [22,23]. The previous calculations of $Li_{0.5}FeF_3$ reported by Doe *et al.* [5] and Zheng *et al.* [6] resulted in a classification as $P4_2/mnm$ space group; however, our structure search found $P4_2nm$ to be the most stable structure. This structure corresponds to the structures reported by Fourquet *et al.* [23] and Lin *et al.* [24], which have alternate Fe^{2+} and Fe^{3+} sites.

Figure 1 shows the lattice constants along the a and b axes [Fig. 1(a)], c axis [Fig. 1(b)], and cell volume [Fig. 1(c)], plotted against the inserted-Li ratio x in trirutile-type Li_xFeF_3. The lattice constants along the a and b axes are at a minimum and that along the c axis is at a maximum at $x = 0.50$. The cell volumes (listed in Table II) are almost constant for $x \leqslant 0.50$; however, they increase for $x > 0.50$.

These results are very much tied to the position of inserted Li. Figure 2 shows the atomic structures of Li_xFeF_3. At $x = 0.25$ and 0.50, inserted Li atoms are located as vacancies in the cation sites of the rutile structure, described as the cation vacancy site (CVS). This CVS converts the rutile structure into a trirutile structure, as described previously. As the CVSs in trirutile-type Li_xFeF_3 correspond to Fe^{2+} sites in the rutile structure, it is expected that similar-sized cations such as Li^+ are relatively easy to insert into the CVS. At $x = 0.75$ and 1.00, inserted Li atoms are located at the IS because the CVSs are already occupied by Li^+. In the present structure models, the most stable structure is obtained by lining up the interstitial Li atoms along the b axis. ISs are narrow sites, in which the bond lengths used to coordinate the F atoms are short; therefore, Li atoms inserted into ISs are expected to have a more significant effect on the local structures of Li_xFeF_3.

After relaxation in the structures, the magnetic orders are qualitatively similar to the initial structures, i.e., antiferromagnetic in $x = 0.00$ and 1.00, and ferrimagnetic in $x = 0.25$ and 0.75. These results are compatible with those of previous experiments [23] and first-principles calculations [13]. For $x = 0.50$, two calculations reported that the antiferromagnetic arrangement was most stable [6,24]; however, the ferrimagnetic arrangement is most stable in our calculation. Lin *et al.* also reported that the total energy of the antiferromagnetic arrangement was 0.50 meV/Fe lower than that of the ferrimagnetic arrangement [24]. In our calculation, however, the total energy of the ferrimagnetic arrangement is 1.3 meV/Fe lower than that of the antiferromagnetic arrangement. These energy differences between the antiferromagnetic and ferrimagnetic arrangements are too small to determine the most stable state with usual DFT calculations, and the optimized lattice constants and internal atomic coordinates of these two magnetic arrangements are almost equivalent in our calculation. We therefore consider that these magnetic arrangements do not affect our discussion.

Here we discuss the details of the local structures in Li_xFeF_3. Table III lists Fe-F distances, Bader charges [26–29], and volumes of FeF_6 octahedra in trirutile-type Li_xFeF_3, rhombohedral FeF_3, and rutile-type FeF_2. The Bader charge is estimated by the integration of the electronic charge density within the Bader region, which is divided into atomic regions where the dividing surfaces have a minimum charge density. It is a simple and useful index, used to analyze the atomic charge state. A comparison of each Fe site at $x = 0.25$ demonstrates that the volume of $Fe1F_6$ octahedra is larger than those of the other Fe sites (Fe2–4). The volume of $Fe1F_6$ octahedra in $Li_{0.25}FeF_3$ is also larger than that in $Li_{0.00}FeF_3$. The expansion of the octahedral volume is a result of the elongations of Fe1-F

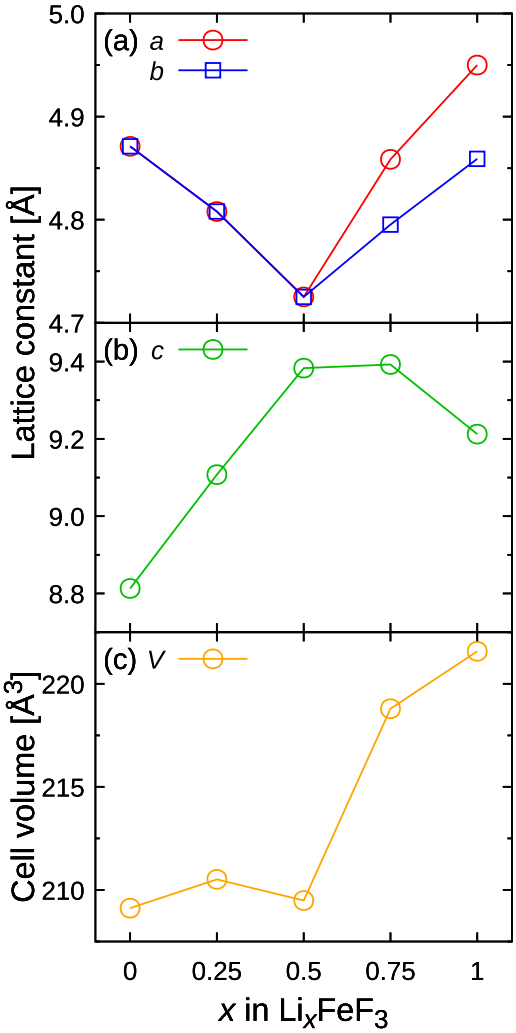

FIG. 1. Lattice constants along the (a) *a* and *b* axes, (b) *c* axis, and (c) cell volumes plotted against the inserted-Li ratio *x*.

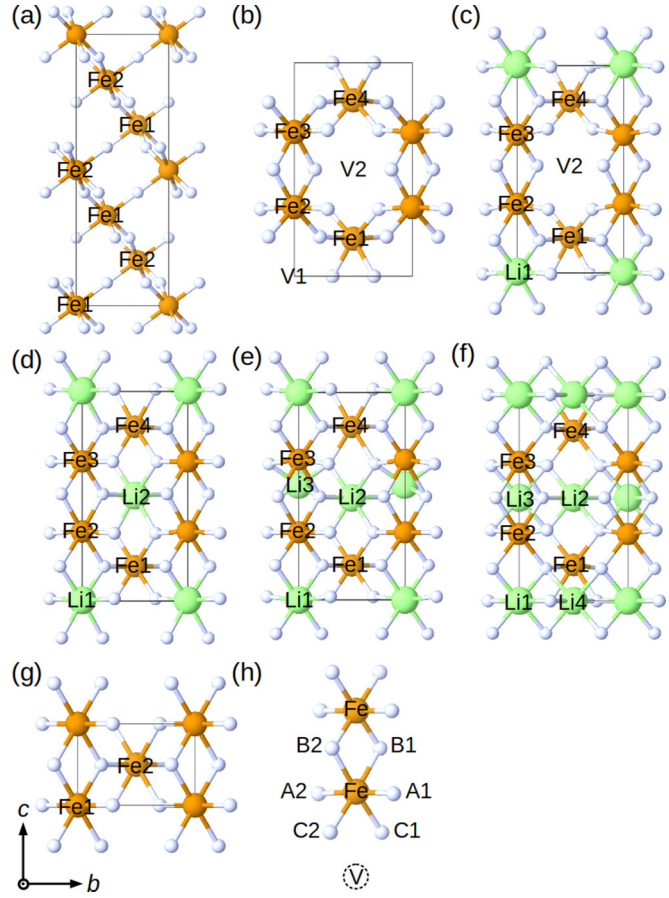

FIG. 2. Atomic structures of (a) rhombohedral FeF_3, and (b)–(f) Li_xFeF_3 ($x = 0-1$), and (g) rutile-type FeF_2. In (h), the labels correspond to the local structure around the Fe site. A1, A2, B1, B2, C1, and C2 indicate the coordination F sites of Fe. We use A1 and A2 for F in the direction of *ab*-in-plane, B1 and B2 for F in the direction of the *c* axis and edge sharing with another Fe site, and C1 and C2 for F in the direction of the *c* axis and edge sharing with the neighbor Li(V) site. V in (b), (c), and (h) indicates the cation vacancy site (CVS). The three-dimensional structures were illustrated using the VESTA [25] software package.

distances. Furthermore, the Bader charge of Fe1 is also greater than those of the other Fe sites. These results indicate that the electron density around Fe1 increases, suggesting that the valency of Fe1 decreases from 3+ to 2+. A comparison with rhombohedral FeF_3 and rutile-type FeF_2 makes this clear. At $x = 0.25$, the Fe-F distances, Bader charges, and volumes of FeF_6 octahedra in Fe1 reveal similar features to those in FeF_2, whereas those of the other Fe sites (Fe2–4) are similar to those in FeF_3. These results demonstrated that for $Li_{0.25}FeF_3$, the formal valency of Fe1 is 2+, while a 3+ valency characterizes the other Fe atoms. As expected, for $x = 0.50$, 0.75, and 1.00, the valencies of Fe2 and Fe4 in $Li_{0.50}FeF_3$, Fe2–4 in $Li_{0.75}FeF_3$, and Fe1–4 in $Li_{1.00}FeF_3$ change from 3+ to 2+. As each Li is inserted, the valency of a single Fe changes from 3+ to 2+.

Table IV lists the Li-F distances, vacancy (V)-F distances, interstitial (I)-F distances, and volumes of $Li(V)F_6$ octahedra in trirutile-type Li_xFeF_3 and LiF. The V1-F distances and $V1F_6$ octahedron volume in $Li_{0.00}FeF_3$ clearly decreases, as demonstrated by the corresponding values of $Li_{0.25}FeF_3$. For $Li_{0.25}FeF_3$, the $V1F_6$ octahedron shrinks to the $Li1F_6$ octahedron owing to the Li insertion, whereas the $Fe1F_6$ octahedron expands, as demonstrated in Table III. As a result, the change of the cell volume of $Li_{0.25}FeF_3$ is offset. A similar situation also occurs at $x = 0.50$, with the cell volume only slightly changing compared with those of $x = 0.00$ and 0.25, as shown in Fig. 1(c). The cell volumes in $x > 0.50$ expand because the Li insertion into the ISs leads to an expansion of the $I1(I2)F_6$ octahedra, in addition to the expansion due to the Fe valence transition.

As mentioned previously, the lattice constants along the *a*- and *b*-axes decrease, and that along the *c* axis increases for $0.00 \leqslant x \leqslant 0.50$. Meanwhile, for $0.50 < x \leqslant 1.00$, those along the *a* and *b* axes increase, and the *c* axis decreases. These trends can be largely explained by the following factors.

(a) Shrinkage of $Li(V)F_6$ octahedra by inserting Li into CVSs.

(b) Elongation and contraction of $Li(V)F_6$ octahedra by inserting Li into ISs.

TABLE III. Bond lengths from Fe to coordination F, bond angles of two Fe-F bonds (∠F-Fe-F), Bader charges of Fe, and volumes of FeF_6 octahedra in trirutile-type Li_xFeF_3, rhombohedral FeF_3, and rutile-type FeF_2. The F1–F4 sites are shown in Fig. 2. A1, A2, B1, B2, C1, and C2 indicate the coordination of F atoms as shown in Fig. 2(h).

		Bond lengths [Å]						Angle [°]		Bader	Volume of
x	Site	A1	A2	B1	B2	C1	C2	∠B1-Fe-B2	∠C1-Fe-C2	charge	FeF_6 [Å^3]
0.00	Fe1–4	1.953	1.953	1.966	1.966	1.931	1.931	75.95	101.46	5.85	9.754
0.25	Fe1	2.102	2.103	2.124	2.205	2.035	1.977	72.37	96.56	6.36	11.973
	Fe2	1.879	1.906	2.015	2.015	1.953	1.953	75.38	84.18	5.95	9.752
	Fe3	1.958	1.958	1.915	1.915	1.992	1.992	80.08	89.16	5.93	9.860
	Fe4	2.012	2.012	1.921	1.947	1.934	1.932	82.74	96.35	5.93	9.988
0.50	Fe1,3	1.942	1.942	1.954	1.954	1.969	1.969	83.47	82.74	5.86	9.888
	Fe2,4	2.042	2.042	2.123	2.123	2.101	2.101	75.56	83.54	6.38	11.915
0.75	Fe1	1.951	1.951	1.932	1.932	2.008	2.008	86.19	83.18	5.97	10.058
	Fe2	2.101	2.101	2.110	2.110	2.070	2.070	80.32	89.44	6.44	12.138
	Fe3	2.079	2.079	2.156	2.156	2.046	2.046	77.84	84.75	6.42	12.000
	Fe4	2.014	2.014	2.172	2.172	2.159	2.159	75.40	78.86	6.46	12.264
1.00	Fe1–4	2.071	2.071	2.133	2.133	2.121	2.121	81.77	86.00	6.39	12.344
FeF_3	Fe1,2	1.938	1.938	1.938	1.938	1.938	1.938		90.01	5.97	9.712
FeF_2	Fe1,2	2.026	2.026	2.138	2.138	2.138	2.138	78.60		6.37	12.104

(c) Elongation of Fe-F bond lengths by the transition from Fe^{3+} to Fe^{2+}.

(d) Anisotropic strain of $Fe^{2+}F_6$ octahedra.

The lattice constants along the a and b axes for $0.00 \leqslant x \leqslant 0.50$ are mainly affected by factors (a) and (c). Although the Fe site expands by a factor (c), a contraction owing to factor (a) occurs twice as much, and as a result, the lattice constants along the a and b axes decrease. The change in the lattice constant along the c axis for $0.00 \leqslant x \leqslant 0.50$ is affected by factor (d) in addition to factors (a) and (c). In the rutile structure, the cations are bonded to each other in the c-axis direction by edge sharing. In the trirutile structure, defects are introduced into the cations of the adjacent sites, and the bond angle changes. When Li is inserted into a CVS, the shared F atoms come close to each other, and the angle formed by the Fe-F bonds narrows (∠C1-Fe-C2 in Table III). As there is almost no change in the Fe-F bond distances, the octahedron extends in the direction of the c axis. In addition, FeF_6 octahedra extend along the c axis by the Jahn-Teller distortion of Fe, which transits from a valence of 3+ to 2+. By these additions, the FeF_6 octahedron anisotropically extends in the c-axis direction, such that the lattice constant along the c axis is greatly increased. The changes in the lattice constants along the a and b axes for $0.50 \leqslant x \leqslant 1.00$ are mainly affected by factors (b) and (c). The IS is narrow in the ab-in-plane direction, and inserted Li atoms push out around the F atoms. Li atoms inserted into an IS are closely aligned with the other Li atoms in the b-axis direction; thus, they seem to repel each other. However, the lattice constant along the a axis elongates more than that along the b axis. As Li atoms aligned along the b axis are bonded to each other by face sharing with three F atoms, the LiF_6 octahedra only slightly

TABLE IV. Bond lengths from Li(V) to coordination F, and volumes of Li(V)F_6 octahedra in trirutile-type Li_xFeF_3 and LiF. A1, A2, B1, B2, B3, and B4 indicate coordination F atoms as shown in Fig. 2(h). V1 and V2 correspond to CVSs, and their internal coordinations are (0.0, 0.0, 0.0) and (0.5, 0.5, 0.5), respectively. I1 and I2 correspond to ISs, and their internal coordinations are (0.5, 0.0, 0.5) and (0.0, 0.5, 0.0), respectively. Li1 and Li2 indicate Li-inserted V1 and V2, and Li3 and Li4 indicate Li-inserted I1 and I2.

		Bond lengths [Å]						Volume of
x	site	A1	A2	B1	B2	B3	B4	Li(V)F_6 [Å^3]
0.00	V1,2	2.233	2.233	2.213	2.213	2.213	2.213	14.529
0.25	Li1	2.068	2.169	1.987	1.987	2.190	2.189	12.117
	V2	2.168	2.189	2.247	2.204	2.171	2.196	14.016
0.50	Li1,2	2.042	2.042	2.063	2.063	2.129	2.129	11.763
	I1,2	1.714	1.714	2.293	2.293	2.380	2.380	12.423
0.75	Li1	2.125	2.125	2.134	2.134	2.054	2.054	12.343
	Li2	2.035	2.035	2.060	2.060	2.064	2.064	11.402
	Li3	1.815	1.815	1.858	1.858	2.714	2.714	11.670
	I2	1.809	1.809	2.268	2.268	2.280	2.280	12.381
1.00	Li1,2	2.076	2.076	2.043	2.043	2.043	2.043	11.463
	Li3,4	1.856	1.856	2.076	2.076	2.076	2.076	10.658
LiF	Li	2.030	2.030	2.030	2.030	2.030	2.030	11.151

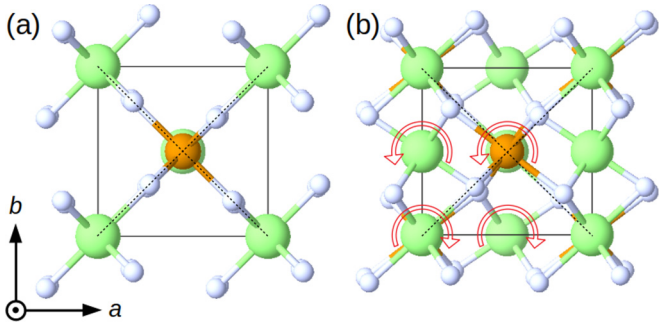

FIG. 3. Atomic structures of (a) $Li_{0.50}FeF_3$ and (b) $Li_{1.00}FeF_3$ viewed from the direction of the c axis.

expand in the direction of the b axis, compared with those at the point or those that are edge sharing. This geometric restriction causes the LiF_6 octahedra to tilt and push out the F atoms in the direction of the a axis [as shown in Figs. 3(a) and (b)]. Finally, the changes in the lattice constant along the c axis for $0.50 \leqslant x \leqslant 1.00$ are mainly affected by factors (b) and (c). As the width of the ISs in the direction of the c axis is as large as that of the CVSs, it contracts by Li insertion. Li3 shrinks between Fe2 and Fe3, and Li4 shrinks between Fe1 and Fe4 [as shown in Fig. 2(f)]. However, it is noteworthy that Li, at the ISs for $x = 0.75$ [Li3 in Fig. 2(e)], is coordinated with four F atoms and bound to $Fe2F_6$ by corner sharing (not edge sharing). Hence, the Li atom does not affect the lattice constant along the direction of the c axis. As a result, the lattice constant along the c axis contracts to the same extent as the a and b axes for $0.00 \leqslant x \leqslant 0.50$, because the factor (b) is the main factor that extends the lattice constant along the c axis.

B. Relative energy

In this section, we discuss the stability of cations in Li_xFeF_3 (Li^+, Fe^{2+}, and Fe^{3+}) relative to stable fluorides (LiF, rutile-type FeF_2, and rhombohedral FeF_3) using relative energy analyses of the calculated models. This analysis can reveal the energetic stability of the structure, in which Li is inserted into Li_xFeF_3. In this system, after the insertion process, the conversion process occurs, which contains FeF_2 and LiF, for example. Therefore, insight into the transition stage is expected through this analysis.

Figure 4 shows the relative energies of Li_xFeF_3 versus x. The relative energies of Li_xFeF_3, E_r, are evaluated by the following formula, with the total energies of rhombohedral FeF_3, rutile-type FeF_2, and LiF as reference:

$$E_r = E(Li_xFeF_3) - xE(LiF) - xE(FeF_2) - (1-x)E(FeF_3), \quad (1)$$

where $E(Li_xFeF_3)$, $E(LiF)$, $E(FeF_2)$, and $E(FeF_3)$ are the total energies of Li_xFeF_3, LiF, rutile-type FeF_2, and rhombohedral FeF_3, respectively. From this formula, Li_xFeF_3 is stable when E_r is negative and unstable when E_r is positive, compared with the three-phase coexistence of LiF, rutile-type FeF_2, and rhombohedral FeF_3. The relative energy at $x = 0.00$, which is equal to the energy difference between rhombohedral FeF_3 and trirutile-type $Li_{0.00}FeF_3$, suggests that rhombohedral FeF_3 is more stable than $Li_{0.00}FeF_3$. For

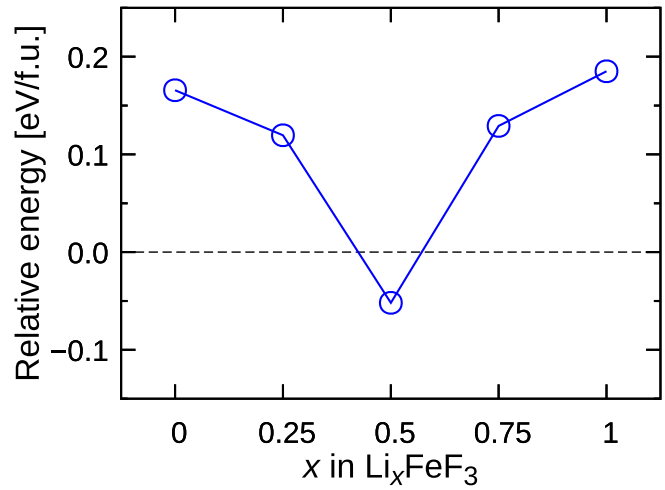

FIG. 4. Relative energies of Li_xFeF_3 evaluated by Eq. (1).

$0.00 \leqslant x \leqslant 0.50$, the relative energy decreases with increasing x; hence, Li insertion occurs easily in a trirutile structure. At $x = 0.50$, the results suggest that $Li_{0.50}FeF_3$ is more stable than the three-phase coexistence as the relative energy is negative. It can be concluded that $Li_{0.50}FeF_3$ is stable from experimental observations [3]. As x increases and is greater than 0.50, the relative energy tends to increase, which leads to a gradual decomposition into $Li_{0.50}FeF_3$, rutile-type FeF_2, and LiF. The increase in relative energy continues until $x = 1.00$. Therefore, the relative energy decreases for $0.00 < x < 0.50$, is a minimum at $x = 0.50$ and increases for $0.50 < x < 1.00$. It is difficult to draw conclusions because the results are calculated with a limited cell size, however $Li_{0.50}FeF_3$ is stable during the process of electrochemical Li insertion into FeF_3, so that $Li_{0.50}FeF_3$ can coexist with FeF_3 for $x < 0.50$ and FeF_2 for $x > 0.50$. The Li_xFeF_3 system becomes unstable as x increases for $x > 0.50$, such that the transition is more stable in rutile-type FeF_2 and LiF (with an accompanying appearance of pure Fe), with simultaneous Li insertion into $Li_{0.50}FeF_3$. Therefore, there is a partial shift to a conversion reaction in this region. This behavior corresponds to a sudden drop in the discharge curve during the electrochemical discharge process, a plateau of up to approximately $x = 0.50$, and a continuous voltage drop at $0.50 < x < 1.00$.

C. Density of states

Figure 5 shows the total DOS and partial DOS (pDOS) for the Fe-d component of rhombohedral FeF_3, rutile-type FeF_2, and trirutile-type Li_xFeF_3. The energy zero is the Fermi level. For each total DOS, there are band gaps in all Li_xFeF_3, and the state of the insulator is maintained as for rutile-type FeF_2 and rhombohedral FeF_3. Rhombohedral FeF_3 [Fig. 5(a)] has a 4-eV band gap and is clearly an insulator. Its valence band maximum (VBM) is formed by the p orbital of F hybridized with the d orbital of Fe, and its conduction band minimum (CBM) is mainly formed by the d orbital of Fe. Note that "orbital" in this study means "orbital component." Rutile-type FeF_2 [Fig. 5(g)] also has a 4-eV band gap, and its CBM is formed by the d orbital of Fe; however, another d orbital of Fe exists immediately

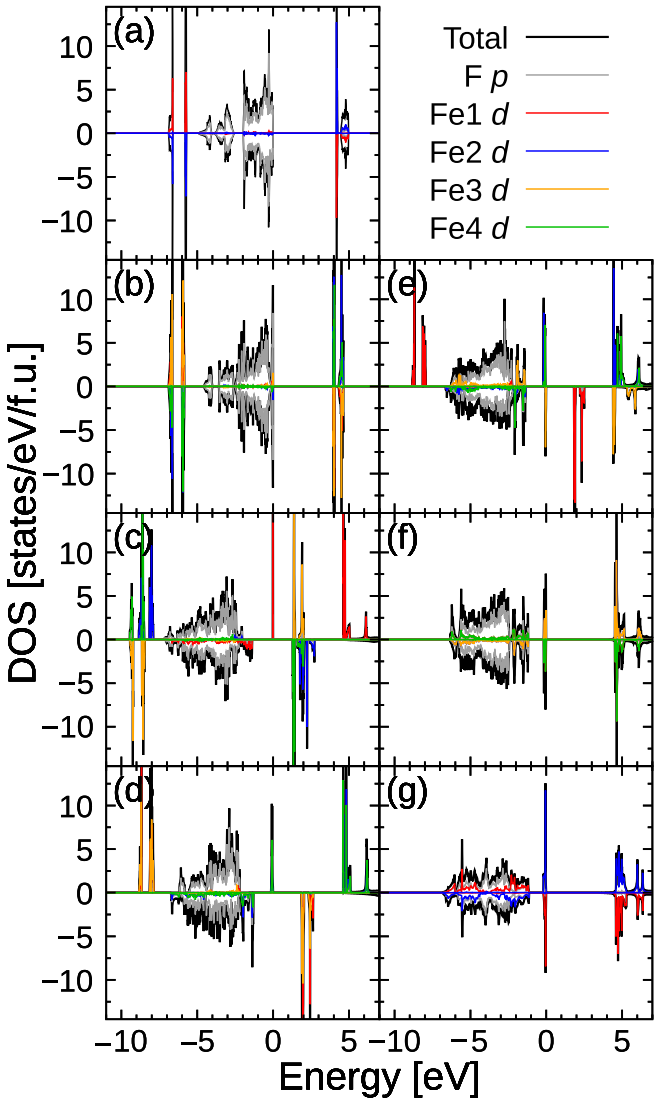

FIG. 5. Density of states of (a) rhombohedral FeF_3, (b) $Li_{0.00}FeF_3$, (c) $Li_{0.25}FeF_3$, (d) $Li_{0.50}FeF_3$, (e) $Li_{0.75}FeF_3$, (f) $Li_{1.00}FeF_3$, and (g) rutile-type FeF_2. Fe2 overlaps with Fe4 in (b)–(f); Fe1 overlaps with Fe3 in (b), (d), and (f).

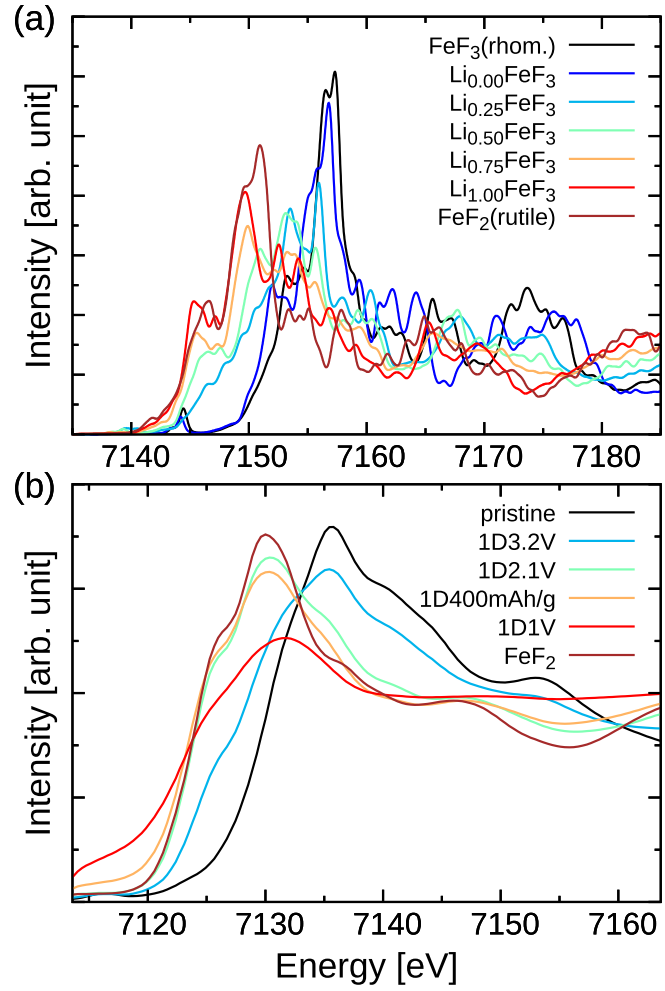

FIG. 6. Fe *K*-edge XANES spectrum (a) calculated by WIEN2K and (b) measured by experiments.

above the *p* orbital of F, immediately under the Fermi level. The DOS of $Li_{0.00}FeF_3$ [Fig. 5(b)] contains approximately the same states of rhombohedral FeF_3, which means that the formal valency of the Fe atoms in both structures are trivalent Fe^{3+}. The pDOS of Fe1 in $Li_{0.25}FeF_3$ [Fig. 5(c)] has *d*-orbital peaks at approximately −2, 0, and 5 eV, similar to the peak position in FeF_2 [Fig. 5(g)]. This indicates that Fe1 is divalent (Fe^{2+}), consistent with the analysis of the atomic structures and Bader charges from the previous section. In contrast, the *d* orbitals of Fe2–4 in $Li_{0.25}FeF_3$ [Fig. 5(c)] are found in a relatively lower position (approximately 2 eV) compared with the Fe pDOS in Figs. 5(a) and 5(b). This is because the *d* orbital of $Fe1^{2+}$ appears in the middle of the band gap between the *p* orbital of F and *d* orbital of Fe, such as the pDOS of FeF_2 [Fig. 5(g)]. This results in a Fermi level increase relative to FeF_3 [Figs. 5(a) and 5(b)], and the band gap is reduced to near 1 eV. The same tendency also occurs for $x = 0.50$ [Fig. 5(d)] and 0.75 [Fig. 5(e)], and as the amount of Li inserted increases, the *d*-orbital component of Fe around the VBM increases. The DOS of $Li_{1.00}FeF_3$ [Fig. 5(f)] has almost the same states as rutile-type FeF_2 [Fig. 5(g)], such that the formal valency of the Fe atoms in both structures are divalent, Fe^{2+}. Each Fe site of Li_xFeF_3 has states similar to rutile-type FeF_2 or rhombohedral FeF_3. The DOS analyses confirmed from the electronic states that Li insertion causes the Fe^{3+} near the inserted Li to be converted into Fe^{2+}, whereas the other Fe^{3+} maintain their states.

D. XANES

Figure 6(a) shows Fe *K*-edge XANES spectra over the entire supercell calculated by the first-principles calculations and the experimental XANES spectra [Fig. 6(b)] measured by operand x-ray absorption fine structure (XAFS) spectroscopy in the first discharge process of FeF_3. Experimental Fe *K*-edge XANES measurements were carried out at BL28XU, SPring-8. The experimental XANES spectra were measured under atmospheric pressure in the transmission mode using ion-chamber detectors. Each lithiated FeF_3 electrode was sealed with a Kapton film, after acquisition from a discharged battery and washing with dimethyl carbonate (DMC) in an

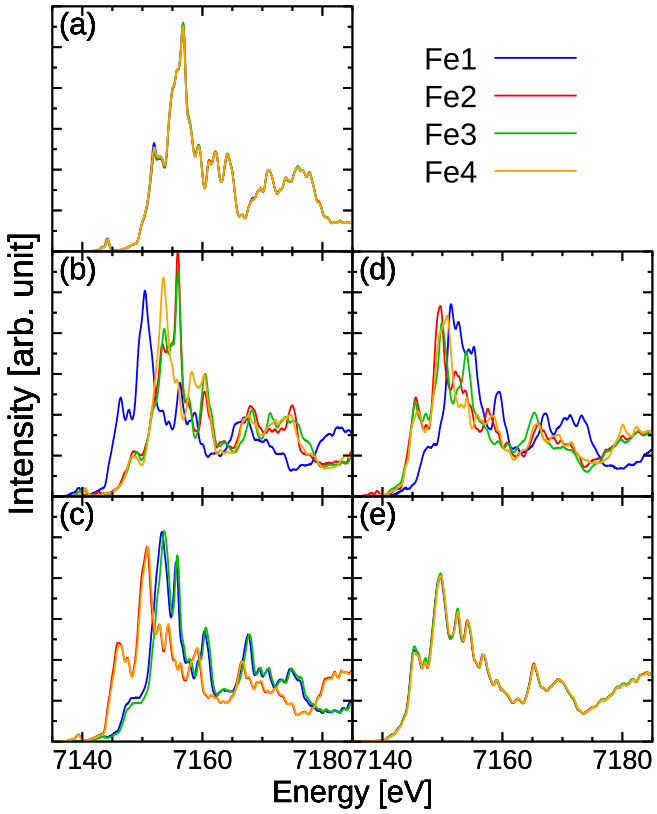

FIG. 7. Fe K-edge XANES spectra of (a) $Li_{0.00}FeF_3$, (b) $Li_{0.25}FeF_3$, (c) $Li_{0.50}FeF_3$, (d) $Li_{0.75}FeF_3$, and (e) $Li_{1.00}FeF_3$.

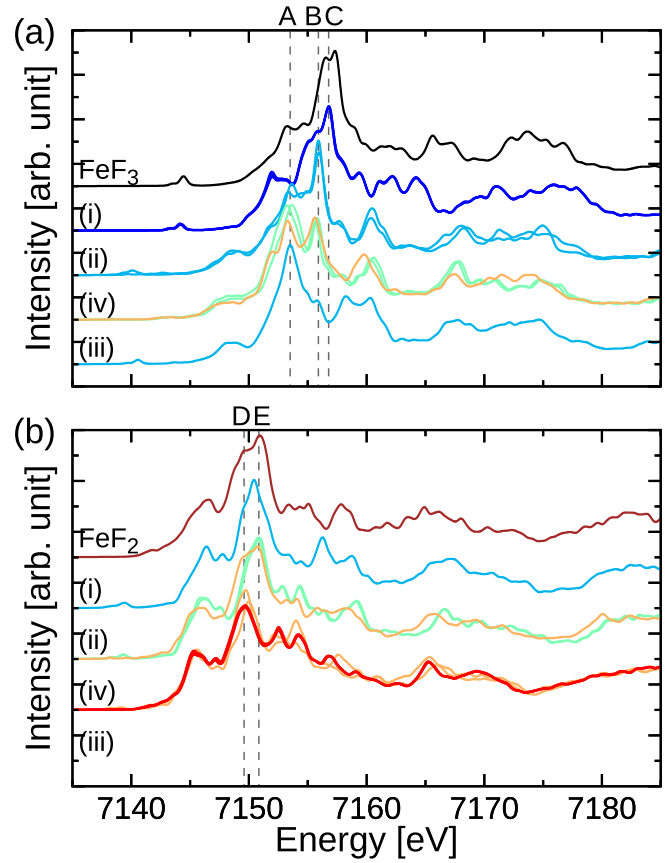

FIG. 8. XANES spectra of the (a) Fe^{3+} and (b) Fe^{2+} sites. The spectra are divided for each category (i)–(iv), and each line color corresponds to the color classification of each composition in Fig. 6.

Ar-filled grove box. In Fig. 6(b), "pristine" and "FeF_2" indicate FeF_3 before the discharge process and bulk FeF_2, respectively; "1D 3.2V" and "1D 2.1V" indicate the intermediate and final states of the Li insertion process into FeF_3, respectively; "1D 400 mAh/g" and "1D 1V" indicate the intermediate and final states of the conversion process, respectively. In the calculated XANES spectra in Fig. 6(a), rhombohedral FeF_3 and rutile-type FeF_2 have main peaks at approximately 7157 and 7151 eV, respectively, and the energy difference between their two peaks is approximately 6 eV. This energy difference value is the same as that of the previous experiment, shown in Fig. 6(b). As shown in Figs. 6(a) and 6(b), on the other hand, the energy positions in the calculated XANES spectra are different from those in the experimental spectra. The reason for this difference will be considered later. As the deviation of the energy difference between the main peaks of calculation and experiment is at most 0.3%, the relative energy differences of the peaks can be determined. Trirutile-type $Li_{0.00}FeF_3$ (blue line) has almost the same main peak and whole shape as rhombohedral FeF_3 (black line), as shown in Fig. 6(a). The main peak of trirutile-type $Li_{1.00}FeF_3$ (red line) is shifted lower from rutile-type FeF_2 (brown line), whereas both XANES shapes are similar. As the amount of Li inserted increases, the main peak of Fe^{3+} tends to decrease, that of Fe^{2+} tends to increase, and the main peaks shift to the low-energy side as a whole. This tendency is consistent with the observed XANES spectra, as shown in Fig. 6(b).

At the Fe^{3+} sites for $x = 0.25$ (light blue line), 0.50 (green line), and 0.75 (orange line), new peaks appear in the middle of the main peaks of Fe^{2+} and Fe^{3+}, in addition to the main peak of rhombohedral FeF_3. Figure 7 shows the Fe K-edge XANES spectra calculated for each Fe site. In Figs. 7(a) and 7(e), the XANES spectra are almost the same for all Fe atoms. The Fe atoms are trivalent in $Li_{0.00}FeF_3$ [Fig. 7(a)] and divalent in $Li_{1.00}FeF_3$ [Fig. 7(e)]. The spectra of the Fe^{2+} sites in $x = 0.25$, 0.50, and 0.75 [Fe1 in Fig. 7(b), Fe2 and Fe4 in Fig. 7(c), and Fe2–4 in Fig. 7(d)] are similar to those for $Li_{1.00}FeF_3$. On the other hand, the spectra of the Fe^{3+} sites at $x = 0.25$, 0.50, and 0.75 [Fe2–4 in Fig. 7(b), Fe1 and Fe3 in Fig. 7(c), and Fe1 in Fig. 7(d)] have new peaks at a lower energy by approximately 2.3 eV in addition to the main peak whose energy is almost the same as that of $Li_{0.00}FeF_3$. The XANES spectra of Li_xFeF_3 are not the simple summation of Fe^{3+} and Fe^{2+}. In particular, a significant change occurs in the spectrum of Fe^{3+}.

Fe sites in the calculated structures have two cation sites that bind, sharing edges in the c-axis direction, and they can be classified into the following four categories:

(i) Fe^{3+} and vacancy (Fe1–4 in $x = 0.00$ and Fe1 in $x = 0.25$);

(ii) Fe^{3+} and Li^+ (Fe2,3 in $x = 0.25$, Fe2,4 in $x = 0.50$, and Fe4 in $x = 0.75$);

(iii) Fe^{2+} and vacancy (Fe4 in $x = 0.25$);

(iv) Fe^{2+} and Li^+ (Fe1,3 in $x = 0.50$ and Fe1–3 in $x = 0.75$).

Figure 8 shows the spectra for each Fe site [Fe^{3+} in Fig. 8(a) and Fe^{2+} in Fig. 8(b)], classified by the above categories. Note that category (iii) in Fig. 8(b) is blank because it does not exist in the structures calculated in this study. In Fig. 8(a), the spectra of Fe^{3+} changes significantly, depending on the adjacent cation sites. The energy of the main peak in $Li_{0.00}FeF_3$ (blue line) is almost equal to that of the rhombohedral FeF_3 (black line); however, their entire shape is not the same. This is clearly due to the difference in the local structure around Fe. The FeF_6 octahedra in rhombohedral FeF_3 are all bonded by point sharing, and the closest cation (Fe–Fe) distance is 3.79 Å, whereas those in $Li_{0.00}FeF_3$ take the local structure of category (i) and the closest cation distance is 3.10 Å. From Table III, the FeF_6 octahedra in rhombohedral FeF_3 are approximately regular, whereas in category (i) they are distinctively distorted, as can be seen from the variation of bond lengths (A1 to C2) and bond angles (∠B1-Fe-B2 and ∠C1-Fe-C2). The differences in the local structure are believed to have some influence on the XANES spectra. Fe2 and Fe3 in $Li_{0.25}FeF_3$ (light blue) have local structures of category (ii) and main peaks at 7156 eV [marked with B in Fig. 8(a)]. This main peak position is lower than those of rhombohedral FeF_3 and $Li_{0.00}FeF_3$. In addition, a new peak appears at 7153 eV [marked with an A in Fig. 8(a)] located in the middle of the main peaks of Fe^{2+} [marked with D and E in Fig. 8(b)] and Fe^{3+} [marked with B and C in Fig. 8(a)]. These two peaks (marked with A and B) appear at Fe1 and Fe3 in $Li_{0.50}FeF_3$ and Fe1 in $Li_{0.75}FeF_3$, which have the local structure of category (iv). The intensity of the new peak at a lower position (marked with A) tends to be higher. In categories (ii) and (iv), the two peaks marked with A and B are closely related to the presence of Li and Fe atoms, and the ratio of the two peak intensities depends on the adjacent Fe charge state. Fe4 in $Li_{0.25}FeF_3$ has a category (iii) local structure, with the main peak at the position marked with A, and does not have peaks marked with C. The Fe^{3+} sites between Fe and vacancy, corresponding to categories (i) and (iii), do not have two simultaneous peaks (marked with A and C), and the energy alignment of the main peak is strongly affected by the charge of the adjacent Fe site. The Fe^{3+} sites between Fe and Li, of category (ii) and (iv), have two simultaneous peaks (marked with A and B); however, their peak intensities are affected by adjacent Fe-site valencies.

On the other hand, compared with the Fe^{3+} site, the influence of the adjacent site on the Fe^{2+} site is very low. At the Fe^{2+} sites, the main peak at 7151 eV [marked with E in Fig. 8(b)] and another peak at 7150 eV [marked with D in Fig. 8(b)] appear. When the adjacent sites are Fe^{3+} and Li^+, category (ii), the main peaks exist at the positions marked with D and E. For the case in which the adjacent sites are Fe^{2+} and Li^+, category (iv), the main peak only appears at the position marked D. Although very slight differences are seen, the overall shapes are also almost the same and are, thus, considered difficult to distinguish experimentally.

As described above, from the spectrum of each site, the Fe^{2+} spectra only changes slightly, owing to the local environment, and does not result in a distinguishable difference. However, Fe^{3+} has a large effect on adjacent cation sites, and a remarkable difference can be found in the energy of the main peak in the Fe K-edge XANES spectra. Therefore, it is conceivable that the local chemical state differs depending on the difference in local structure among the same Fe^{3+} sites, which is expected to be a useful indicator of a conversion reaction.

We now discuss why the energy positions of the calculated XANES spectra are different from those of the experimental spectra. In this study, we perform a first-principles calculation based on the GGA functional, as described in the theoretical method section, which includes an insufficiency of many-body interactions. Usually the scheme of the on-site Coulomb interaction (GGA + U) is introduced for the strong d-d interaction among Fe atoms. Referring to previous studies [5,6] and after checking ourselves, we adopted $U_{\mathrm{eff}} = 5\,\mathrm{eV}$ in this work. As discussed in previous sections, the current conditions work well for the structure optimizations and electronic states retrieval. On the other hand, the calculation of the XANES spectra requires the electronic states, during excitation. Moreover, the absolute value of the energy window for the Fe K-edge is greater than 7100 eV; thus, the deviation of the energy position shift of the XANES spectra between the calculation and experimental results appears to be relatively larger. However, this deviation is at most 0.3%, and the relative energy difference is in good agreement for both cases as discussed above. Therefore, the relative energy difference between the main peaks of the XANES spectra obtained from the current first-principles calculations can be investigated with experimental XANES spectra.

IV. CONCLUSION

We performed a first-principles calculations for Li insertion into the FeF_3 system and clarified the local chemical state during the initial discharge process based the Li proportion. By Li insertion, rhombohedral FeF_3, a stable structure, is changed from the early stage to trirutile-type Li_xFeF_3. Some Fe atoms near the inserted Li atoms are converted from Fe^{3+} to Fe^{2+}, depending on the insertion number of Li. This was confirmed by a Bader charge analysis around Fe and volume analysis of FeF_6 octahedra. For $x \leqslant 0.50$, the relative energies of Li_xFeF_3 decrease as the inserted Li atoms increase, and the total cell volumes are unchanged owing to the local volume adjustment, expansion of $Fe^{2+}F_6$ octahedra, and shrinking of LiF_6 octahedra, by Li insertion. In particular, $Li_{0.50}FeF_3$ is energetically stable and Li insertion naturally proceeds to this composition under the discharge condition. On the other hand, for $x > 0.50$, Li_xFeF_3 is energetically unstable and the cell volumes also expand. Therefore, there is a partial shift to a conversion reaction in this region. A DOS analysis shows the differences in the electronic states of Fe^{3+} and Fe^{2+} in Li_xFeF_3, with Li insertion from the comparison of rhombohedral FeF_3 and rutile-type FeF_2. In the XANES analysis for Fe K-edge spectra, we demonstrated that the local chemical state has a dependence on the difference of the local structure among the same Fe^{3+} sites, whereas the Fe^{2+} sites are almost the same. Furthermore, the variation of XANES spectra can be clearly categorized into four categories, as discussed in Sec. III D. The results and discussion presented in this study provide important guidelines for clarifying the conversion/reverse conversion reaction for FeF_3 systems in the near future.

ACKNOWLEDGMENTS

This work was supported by the Research and Development Initiative for Scientific Innovation of New Generation Batteries 2 (RISING2) project from the New Energy and Industrial Technology Development Organization (NEDO). The synchrotron radiation experiments were performed at the BL28XU in SPring-8 with the approval of the Japan Synchrotron Radiation Research Institute (JASRI) (Proposals No. 2016A7601 and No. 2016B7607).

[1] H. Arai, S. Okada, Y. Sakurai, and J. Yamaki, Cathode performance and voltage estimation of metal trihalides, J. Power Sources **68**, 716 (1997), proceedings of the Eighth International Meeting on Lithium Batteries.

[2] K. Kumagae, K. Okazaki, K. Matsui, H. Horino, T. Hirai, J. Yamaki, and Z. Ogumi, Improvement of cycling performance of FeF_3-based lithium-ion battery by boron-based additives, J. Electrochem. Soc. **163**, A1633 (2016).

[3] N. Yamakawa, M. Jiang, B. Key, and C. P. Grey, Identifying the local structures formed during lithiation of the conversion material, iron fluoride, in a Li ion battery: A solid-state NMR, X-ray diffraction, and pair distribution function analysis study, J. Am. Chem. Soc. **131**, 10525 (2009).

[4] F. Badway, F. Cosandey, N. Pereira, and G. G. Amatucci, Carbon metal fluoride nanocomposites: High-capacity reversible metal fluoride conversion materials as rechargeable positive electrodes for Li batteries, J. Electrochem. Soc. **150**, A1318 (2003).

[5] R. E. Doe, K. A. Persson, Y. S. Meng, and G. Ceder, First-principles investigation of the Li–Fe–F phase diagram and equilibrium and nonequilibrium conversion reactions of iron fluorides with lithium, Chem. Mater. **20**, 5274 (2008).

[6] Y. Zheng, R. Li, S. Wu, Y. Wen, Z. Zhu, and Y. Yang, First-principles investigation on the lithium ion insertion/extraction in trirutile Li_xFeF_3, Electrochemistry **81**, 12 (2013).

[7] A. Kitajou, I. Tanaka, Y. Tanaka, E. Kobayashi, H. Setoyama, T. Okajima, and S. Okada, Discharge and charge reaction of perovskite-type MF_3 (M = Fe and Ti) cathodes for lithium-ion batteries, Electrochemistry **85**, 472 (2017).

[8] P. E. Blöchl, Projector augmented-wave method, Phys. Rev. B **50**, 17953 (1994).

[9] G. Kresse and D. Joubert, From ultrasoft pseudopotentials to the projector augmented-wave method, Phys. Rev. B **59**, 1758 (1999).

[10] G. Kresse and J. Hafner, Ab initio molecular dynamics for liquid metals, Phys. Rev. B **47**, 558 (1993).

[11] G. Kresse and J. Furthmüller, Efficient iterative schemes for ab initio total-energy calculations using a plane-wave basis set, Phys. Rev. B **54**, 11169 (1996).

[12] S. López-Moreno, A. H. Romero, J. Mejía-López, A. Muñoz, and I. V. Roshchin, First-principles study of electronic, vibrational, elastic, and magnetic properties of FeF_2 as a function of pressure, Phys. Rev. B **85**, 134110 (2012).

[13] R. F. Li, S. Q. Wu, Y. Yang, and Z. Z. Zhu, Structural and electronic properties of Li-ion battery cathode material FeF_3, J. Phys. Chem. C **114**, 16813 (2010).

[14] J. E. Jørgensen and R. I. Smith, On the compression mechanism of FeF_3, Acta Crystallogr. B **62**, 987 (2006).

[15] J. W. Stout and S. A. Reed, The crystal structure of MnF_2, FeF_2, CoF_2, NiF_2 and ZnF_2, J. Am. Chem. Soc. **76**, 5279 (1954).

[16] E. O. Wollan, H. R. Child, W. C. Koehler, and M. K. Wilkinson, Antiferromagnetic properties of the iron group trifluorides, Phys. Rev. **112**, 1132 (1958).

[17] D. P. Belanger and H. Yoshizawa, Neutron scattering and the critical behavior of the three-dimensional ising antiferromagnet FeF_2, Phys. Rev. B **35**, 4823 (1987).

[18] J. P. Perdew, K. Burke, and M. Ernzerhof, Generalized Gradient Approximation Made Simple, Phys. Rev. Lett. **77**, 3865 (1996).

[19] S. L. Dudarev, G. A. Botton, S. Y. Savrasov, C. J. Humphreys, and A. P. Sutton, Electron-energy-loss spectra and the structural stability of nickel oxide: An LSDA+U study, Phys. Rev. B **57**, 1505 (1998).

[20] H. J. Monkhorst and J. D. Pack, Special points for Brillouin-zone integrations, Phys. Rev. B **13**, 5188 (1976).

[21] P. Blaha, K. Schwarz, G. K. H. Madsen, D. Kvasnicka, J. Luitz, R. Laskowski, F. Tran, and L. D. Marks, *WIEN2k, An Augmented Plane Wave + Local Orbitals Program for Calculating Crystal Properties* (Karlheinz Schwarz, Technische Universität Wien, Austria, 2018).

[22] P. Josik, A. Tressaud, R. de Pape, and P. Hagenmuller, Etude cristallographique et magnétique d'un fluorure inédit de type trirutile, C. R. Acad. Sci. C **267**, 1711 (1968).

[23] J. Fourquet, E. L. Samedi, and Y. Calage, Le trirutile ordonné $LiFe_2F_6$: Croissance cristalline et étude structurale, J. Solid State Chem. **77**, 84 (1988).

[24] L.-F. Lin, Q.-R. Xu, Y. Zhang, J.-J. Zhang, Y.-P. Liang, and S. Dong, Ferroelectric ferrimagnetic $LiFe_2F_6$: Charge-ordering-mediated magnetoelectricity, Phys. Rev. Mater. **1**, 071401 (2017).

[25] K. Momma and F. Izumi, *VESTA3* for three-dimensional visualization of crystal, volumetric and morphology data, J. Appl. Crystallogr. **44**, 1272 (2011).

[26] G. Henkelman, A. Arnaldsson, and H. Jónsson, A fast and robust algorithm for Bader decomposition of charge density, Comput. Mater. Sci. **36**, 354 (2006).

[27] E. Sanville, S. D. Kenny, R. Smith, and G. Henkelman, Improved grid-based algorithm for Bader charge allocation, J. Comput. Chem. **28**, 899 (2007).

[28] W. Tang, E. Sanville, and G. Henkelman, A grid-based bader analysis algorithm without lattice bias, J. Phys.: Condens. Matter **21**, 084204 (2009).

[29] M. Yu and D. R. Trinkle, Accurate and efficient algorithm for Bader charge integration, J. Chem. Phys. **134**, 064111 (2011).